Iranian Journal of Hydrogen & Fuel Cell 2(2021) 77-93

Iranian Journal of Hydrogen & Fuel Cell

IJHFC

Journal homepage://ijhfc.irost.ir

Comparative Numerical Study of Co- and Counter-Flow Configurations of an All-Porous Solid Oxide Fuel Cell

Majid Kamvar[1,*]

[1] **Department of Mechanical Engineering, Parand Branch, Islamic Azad University, Parand, Iran**

Article Information

Article History:

Received:
18 Feb 2021
Received in revised form:
16 May 2021
Accepted:
21 May 2021

Keywords

Hydrogen
Solid Oxide Fuel Cell
All-porous
Flow geometry

Abstract

The All-Porous Solid Oxide Fuel Cell is a concept in which the electrolyte layer, similar to the other two layers, is porous. Thus, firm sealing between cell layers is not a concern, and fuel and oxidant are free to intermix through the porous electrolyte. Furthermore, The All-Porous Solid Oxide Fuel Cell does not need any sealant, and crack generation in its electrolyte component does not terminate cell operation. Cell performance enhancement, based on the flow geometry, is the main target of this study. To achieve this goal, two flow configurations, co-flow and counter-flow, are considered and compared for a hydrogen-fuelled planar All-Porous Solid Oxide Fuel Cell. A finite element method-based commercial software is utilized to solve the nonlinear governing equations of mass, momentum, energy, charge balance, and gas-phase species coupled with kinetics equations. The results include velocity field distribution, species mole fraction in different layers, and temperature contours within the cell. Results show that the counter flow configuration concept reveals better cell performance.

1. Introduction

Fuel cells are an efficient technology for generating electricity through the direct electrochemical conversion of a fuel and an oxidant without thermal conversion [1]. SOFCs are gaining considerable attention due to their high efficiency and fuel flexibility [2-6]. SOFCs work at high temperatures, between 500 and 950°C [7]. These high operating temperatures have both advantages and disadvantages. On the one hand,

*Corresponding author. *mkamvar@mail.kntu.ac.ir

doi: 10.22104/ijhfc.2021.4712.1212

above 650°C, they permit direct internal reforming of simple hydrocarbons at the anode as well as the fuel flexibility of using hydrogen, carbon monoxide, and simple hydrocarbon fuels in one device. On the other hand, they can lead to thermal stresses, especially during thermal cycling, that might lead to crack formation within SOFC components [8]. The high operating temperature also gives rise to increased materials degradation, as far as this is thermally activated [9-12]. In dual chamber SOFCs, the key requirement of strict separation of fuel and oxidant [13requires reliable sealing between the electrode compartments [14]. One way to simplify the cell structure is to use a single chamber instead of two fully separated chambers and simultaneously expose a uniform mixture of fuel and oxidant gases to both the anode and cathode. This simplified design is called a single chamber solid oxide fuel cell (SC-SOFC) and was demonstrated by Hibino and Iwahara for the first time in 1993 [15].

Compared to conventional SOFCs, SC-SOFCs, have the advantage of a lower weight, smaller volume (especially with the planar type), and also remove the need for complex sealants. Thus, the manufacturing process is potentially more cost-effective. However, the presence of 'spectator' species at the two functional layers of SC-SOFCs (i.e., the transport of hydrogen to the cathode functional layer with no chemical interaction) leads to very low performance compared to conventional SOFCs due to reactant dilution [16]. A number of studies on SC-SOFC have been performed using numerical approaches to enhance this low performance [2, 9, 12-27]. Reported SC-SOFC performances show that high power density and high fuel efficiency cannot be achieved simultaneously in an SC-SOFC. This is due to flammability and flow pattern issues. Among these studies, Kamvar et al. [2] compared different anode and cathode configurations of SC-SOFC. Their results revealed that Ohmic losses played a key role in improving cell performance. In their recent work, Kamvar et al. [16] numerically investigated the effect of different support types on cell performance. Their results showed that the anode-supported scheme showed the best performance compared to the other two support types. They also reported that a lack of oxygen on the cathode side of a cathode-supported cell was an obstacle that limited the cell performance in open circuit voltage conditions. Many useful reports have been published in the area of dual chamber SOFCs. However, a number of novel numerical studies have recently been conducted in the SOFC area. Kong et al. [28] proposed a novel interconnector design called the X-type interconnect. Their numerical results showed that a cell with this novel design presented a better performance compared to a cell with conventional interconnection. Schluckner et al. [29] studied the influence of different possible flow configurations and electrical contact positions on the temperature distribution within the cell. They claimed that it was not possible to move the maximum cell temperature to the cell center by way of varying the electrical contact positions. Moreno-Blanco et al. [30] numerically studied the effect of the channel-electrode interface area on the performance of planar SOFC. They found that the size (width) and number of channels in a co-flow arrangement had a direct effect on cell performance.

Guo et al. [31] successfully designed a novel concept of dual chamber SOFC technology with a porous electrolyte called the All Porous Solid Oxide Fuel Cell (AP-SOFC) that forms a link between the dual and single chamber SOFCs. Their cell used methane fuel without any external reformer or steam addition. The porous structure of the electrolyte allowed gaseous species transport through the electrolyte. Therefore, the presence of cracks in the electrolyte or sealant failure is of no concern in AP-SOFCs, and fuel-oxygen concentration management is performed easily to keep the system from the risk of explosion. An experimental study by Guo et al. presented Xu et al.'s [32] developed numerical models for button AP-SOFC. Their results focused on electrolyte porosity optimization to control the oxygen transport to the anode in

order to prevent the risk of simple combustion (and explosion) as well as methane coking and carbon deposition in the anode, which would considerably reduce the cell performance. In another study, Xu et al. [33] investigated the thermal effects in AP-SOFC. They conducted parametric studies for various operating parameters such as voltage, inlet gas temperature, and different cell structures to optimize cell performance. The aim of this study is to present a numerical model of a planar hydrogen-fuelled AP-SOFC to examine the flow configuration effect on the cell performance for the first time. Using hydrogen as the fuel has the advantages of i) avoiding coking problems and ii) simplifying the overall anode chemistry. However, the leakage flow through the porous electrolyte can decrease cell performance. Thus, the chief purpose of this paper is to compare co- and counter-flow configurations in order to report the which flow configuration is better for the all-porous scheme.

2. Problem Definition

A 2D numerical steady-state condition model was used to predict the performance of a planar AP-SOFC. In the planar type of AP-SOFC, the porous electrolyte is sandwiched between two porous electrodes. As shown in Fig.1, two fully separated chambers are used to feed fuel and oxidant individually, and the porous structure of the electrolyte allows the gaseous species to transport from anode to cathode and vice versa. The cell consists of five layers; an anode current collecting layer made of nickel (Ni), an anode functional layer made of a cermet of nickel with yttria-stabilized zirconia (50%Ni-50%YSZ), a porous electrolyte of YSZ, a cathode functional layer made of a composite of YSZ and lanthanum strontium manganite (50%YSZ-50%LSM), and a cathode current collection layer of pure LSM. To present a more realistic prediction of the cell performance, all geometrical, micro-structural, and thermo-physical parameters of the current cell follow the experimental base case reported by Timurkutluk et al. [34]. The geometrical data of the model considered in this study are tabulated in Table 1. A 0.3 electrolyte layer porosity is applied to the AP-SOFC scheme. As stated, two flow configurations named co- and counter-flow, as shown in Fig. 2 were used to compare their performance with each other.

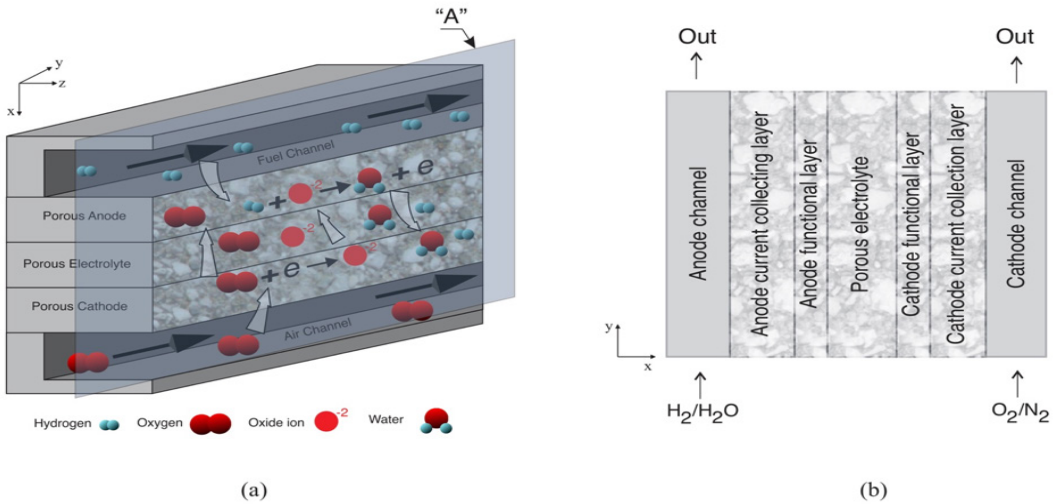

(a) (b)

Fig. 1. (a) Schematic illustration of a single cell of planar-type AP-SOFC, (b) cross-section of planar-type AP-SOFC, which represents the computational domain (detailed "A") .

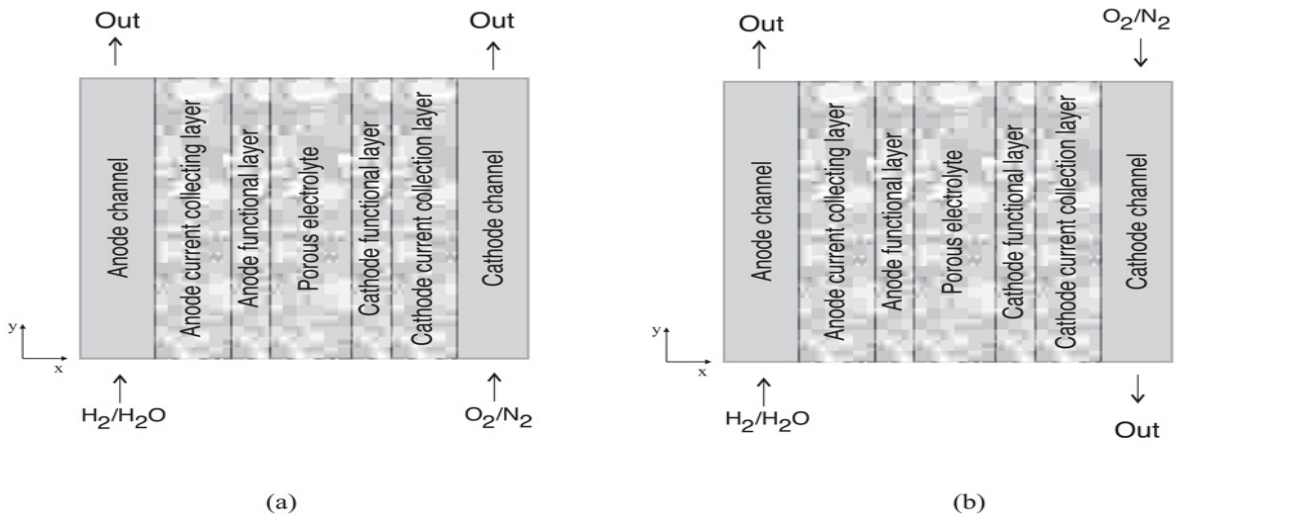

Fig. 2. Schematic illustration of two different flow configurations used in this study: (a) Case 1: Co-flow planar AP-SOFC, (b) Case 2: Counter-flow Planar AP-SOFC.

The governing equations for gas-phase species, energy, momentum, and charge balance are coupled with kinetics equations, which describe the electrochemical reactions.

Table1. Geometrical Data

Description	Symbol	Value
Channel length	L_{ch}	10 [mm]
Channel height	H_{ch}	0.5 [mm]
Anode current collecting layer thickness	t_a	50 [μm]
Anode functional layer thickness	t_{af}	20 [μm]
Electrolyte thickness	t_e	50 [μm]
Cathode current collector thickness	t_c	50 [μm]
Cathode functional layer thickness	t_{cf}	20 [μm]

The simplifying assumptions of the current study are listed in the following:

- Steady-state conditions.
- The electrodes are selective; this means that the following reactions specifically occur at the two electrodes, respectively.

Anode oxidation of hydrogen:

$$^{-}H_2+O^{-2} \rightarrow H_2O+2e \quad (1)$$

Cathode reduction of oxygen:

$$O_2+ 2e^{-} \rightarrow O^{-2} \quad (2)$$

- Flow is two-dimensional, compressible, and laminar with a Mach number lower than 0.3.
- All species behave as an ideal gas.
- The inertia term in porous media flow is neglected (Stokes-Brinkman's assumption).
- The thermal diffusion is disregarded.
- The Ohmic resistance due to electron transport is neglected since the electronic conductivity of the electrodes is noticeably high compared to the ionic conductivity.
- Thermal equilibrium is upheld between solid and fluid phases in the porous electrodes and electrolyte.
- The flammability of hydrogen in air is negligible.

The governing equations are described separately below.

2.1. Conservation of mass and momentum

The continuity equation for compressible fluids is stated as [35 and 36].

$$\nabla.(\rho u) = 0 \tag{3}$$

where ρ is the density of the mixture, and u is the velocity vector. ε is the porosity of the porous electrodes and electrolyte with a value between 0 and 1. Considering free fluid flow inside the chamber, the continuity equation is obtained by setting the porosity value to unity.

The single-phase fluid flow equation for a compressible flow in porous electrodes using Darcy's law is expressed as [35-37]:

(4)

$$\frac{\rho}{\varepsilon}\left((u.\nabla)\frac{u}{\varepsilon}\right) = \nabla.\left(-pI + \frac{\mu}{\varepsilon}(\nabla u + (\nabla u)^T) - \frac{2\mu}{3\varepsilon}(\nabla u)I\right) + \rho g - \left(\frac{\mu}{K}\right)u + F$$

where μ is the dynamic viscosity of the fluid, ε and κ are the porosity and permeability of the porous electrodes and electrolyte, respectively, and F is the volume force acting on the fluid. By applying Stokes-Brinkman's assumption, the inertial term ($(u.\nabla)\frac{u}{\varepsilon}$) in the porous electrode and electrolyte flow vanish. In a free media gas chamber, porosity ε is taken to be unity, while permeability κ is infinite. The dynamic viscosity of a multicomponent mixture, , is obtained by [38]:

$$\mu_f = \sum_j x_j \mu_j \tag{5}$$

where μ_j is the dynamic viscosity of the jth species of the mixture and x_j is its mole fraction.

2.2. Species conservation

The governing equation of species conservation for an individual species i can be written as [38]:

$$\nabla.j_i + \rho(u.\nabla)\omega_i = R_i \tag{6}$$

where j_i is the relative mass flux vector, ω_i is the mass fraction of the ith species, and R_i is the source term that accounts for mass deposit or mass creation of the ith species. By applying the Maxwell-Stefan diffusion model, the relative mass flux vector can be written as [39]:

$$j_i = -\rho\omega_i \sum_k D_{ik} d_k \tag{7}$$

where d_k is the diffusional driving force and D_{ik} are the multicomponent Fick's diffusivities calculated by [39]:

(8)

$$D_{ik} = 1.883\times10^{-2} T^{1.5} (1/M_i + 1/M_k)^{1/2} / (p\sigma_{ik}^2 \Omega_D)$$

where σ is the characteristic length in Angstrom and Ω_D is the diffusion collision integral. The multicomponent Fick's diffusivities are corrected to account for mass transfer resistance in the porous electrodes and electrolyte according to the following equation:

$$D_{ik}^{eff} = (\varepsilon/\tau) D_{ik} \tag{9}$$

where τ is the tortuosity of porous media.

2.3. Charge conservation

By applying Ohm's law, ionic and electronic charge conservation equations are stated as [40]:

$$-\nabla.(\sigma_e \nabla \phi_e) = j_e \tag{10}$$

$$-\nabla.(\sigma_i \nabla \phi_i) = j_i \tag{11}$$

respectively, where σ_e and σ_i are the electronic and ionic conductivity and Φ_e and Φ_i are the electric and ionic potential, respectively.

The right-hand sides of equations (10) and (11) describe electrical and ionic charge source/sink terms, respectively, and only exist in the anode and cathode functional layers. According to equations (1) and (2), electrons and ions are produced in the anode and cathode functional layers, respectively. The electrical and ionic charge source for the anode functional layer are the sink and source terms, whereas, for the cathode layer, they are the source and sink terms, respectively. Consequently, the sink and source term of the charge conservation equation for the anode and cathode layers are stated using the Butler-Volmer equation [41-43]:

$$j_{i,a} = -j_{e,a} = A_a j_{o,a}[\exp(n\alpha_a F\eta_{act,a}/R_u T) - \exp(-n(1-\alpha_a)F\eta_{act,a}/R_u T)] \tag{12}$$

$$j_{e,c} = -j_{i,c} = A_c j_{o,c}[\exp(n\alpha_c F\eta_{act,c}/R_u T) - \exp(-n(1-\alpha_c)F\eta_{act,c}/R_u T)] \tag{13}$$

where A is the electrochemically active surface area per unit volume, α is the charge transfer coefficient whose value lies between 0 and 1, F is Faraday's constant (equal to 96487 C/mol), and η_{act} is the activation overpotential. The indexes "a" and "c" in the above equations denote the anode and cathode sides. The anode and cathode side activation overpotentials are calculated by [15]:

$$\eta_{act,a} = \phi_e - \phi_i \tag{14}$$

$$\eta_{act,c} = \phi_e - \phi_i - V_{oc} \tag{15}$$

respectively, where V_{oc} is the open circuit voltage calculated by the Nernst equation [44]:

$$V_{oc} = 1.317 - 2.769\times10^{-4}T + R_u T/2F \ln(p_{H_2}.po_2^{1.2}/p_{H_2O}.po_{ref}^{1.2}) \tag{16}$$

In Eqs (14) and (15), j_0 is the exchange current density which is related to the system total pressure (p_t) by [43]:

$$j_{o,c} = j^*_{o,c}\frac{(p_{O_2}/p^*_{O_2})^{1/2}}{1+(p_{O_2}/p^*_{O_2})^{1/2}} \tag{17}$$

for the cathode side and

$$j_{o,a} = j^*_{o,a}\frac{(p_{H_2}/p^*_{H_2})^{1/4}(p_{H_2O})^{3/4}}{1+(p_{H_2}/p^*_{H_2})^{1/2}} \tag{19}$$

for the anode side. In which is partial pressure of ith species and is related to the system total pressure using Dalton's law of partial pressure by [45]:

$$p_i = x_i p_t \quad (18)$$

$j^*_{o,c(a)}$ and $p^*_{O_2(H_2)}$ in Eqs (19) and (20) are the material- and temperature-dependent characteristic constants that are reported in an Arrhenius form in Huang and Goodenough [43].

It is worth mentioning that ion transport physics is active for the anode and cathode functional layers as well as the electrolyte, while electron transport physics is valid for both electrode functional layers, as well as the anode substrate and cathode current collection layers.

2.4. Energy conservation

The conservation of energy for the entire domain under steady state conditions is governed by [46]:

$$\nabla.(\rho C_p u T - k \nabla T) = Q \quad (20)$$

Where C_p is the specific heat, k is the thermal conductivity, and Q is the energy source term due to ionic transport resistance and reversible and irreversible heat generation. In order to account for the porosity of the electrodes, the effective relationship is used for specific heat capacity (ρC_p) and thermal conductivity (k) by applying the thermal equilibrium between solid and fluid phases in porous electrodes [35, 46]:

$$(\rho C_p)_{eff} = \varepsilon(\rho C_p)_f + (1-\varepsilon)(\rho C_p)_s \quad (21)$$

$$k_{eff} = \varepsilon k_f + (1-\varepsilon) k_s \quad (22)$$

In the above equations, the indexes “f” and “s” denote fluid and solid phase, respectively. Specific heat and conductivity for the fluid mixture is determined by:

$$C_{p,f} = \sum_j \omega_j C_{p,j} \quad (23)$$

$$k_f = \sum_j x_j k_j \quad (24)$$

Where $C_{p,j}$ and k_j are the specific heat and conductivity for each gas species, respectively, and x and ω are the mole and mass fraction, respectively.

2.5. Boundary conditions

Specifying the boundary conditions for each physics was necessary to fulfill the mathematical modeling. Two types of boundary conditions were used: the Dirichlet boundary condition in which the value of the dependent variable was specified, and the Neumann boundary condition in which the derivative of the dependent variable was specified.

At the inlet of the chamber, velocity, mole fraction of species, and temperature were specified. At the chamber walls, no-slip (u=0) and thermal insulation boundary conditions were applied for fluid flow and energy equations, respectively, and the insulation boundary condition was used for transport of species equations. At the outlet of the chamber, the pressure was equal to the total pressure, and conduction heat transfer in comparison to convection heat transfer was neglected. Similarly, the diffusion term in the species transport equation was disregarded versus the convection term. At the intersection between electrodes and the gas channel, the voltage was specified. In other words, the cell voltage and ground voltage were applied for cathode-channel and anode-channel intersections, respectively. Since the porous electrolyte was only impermeable to electron transport, the insulation boundary condition was used for electron transport

equations at all exterior boundaries of the electrolyte layer. Furthermore, since it was assumed that the electrochemical reactions occur in the functional layers, the insulation boundary condition was utilized for the ion transportation physics at the electrodes-functional layer interfaces. The continuity boundary condition was applied for the rest of the boundary conditions.

3. Numerical procedure

The governing equations were solved through finite element analysis in the commercial software COMSOL MULTIPHYSICS®. A triangular mesh was chosen. The mesh distribution was such that more elements were concentrated in the functional layers where more calculation volume existed. To capture instabilities occurring in the solution procedure, the governing equations were solved in steps. Since the Butler-Volmer and fluid flow equations are non-linear equations, the ionic and electronic current distributions were obtained initially then the fluid flow equations were solved. Finally, all governing equations were solved fully coupled. The solution for each step was stored and applied as an initial guess for the next step. Linear elements were used for all the dependent variables. A relative tolerance of 1×10^{-6} was chosen. To show how mesh size affects the model accuracy, a mesh dependency study was done and is shown in Fig. 3 and Table 2. To have both accuracy and time-saving in the solution procedure, mesh type 3 with 237830 linear elements was chosen. The calculations were performed on a laptop with the following specifications: processor Intel (R) Core ™ i7 CPUX980 @ 2.2 GHz with an installed RAM of 16 GB.

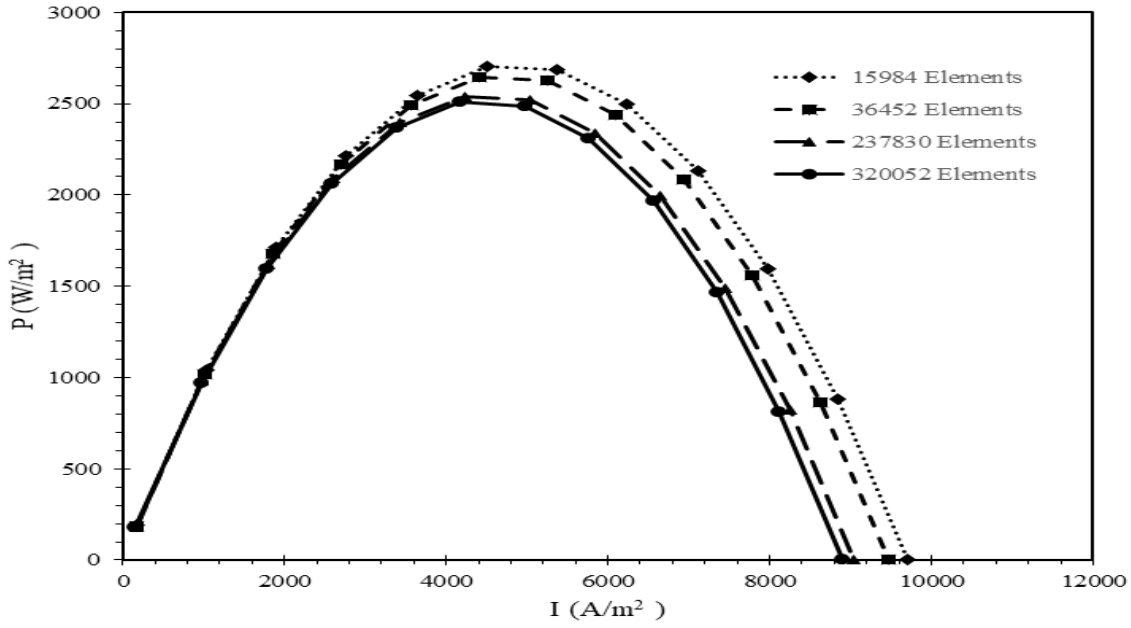

Fig. 3. Effect of mesh sizes on model accuracy.

Table 2. Mesh types effect on maximum power density evaluation and solution time.

Mesh types	Elements no.	Max power density (W/m²)	Solution time
Mesh 1	15984	2703.2	1 min 16s
Mesh 2	36424	2642.6	2 min 36
Mesh 3	237830	2540.1	17 min 41s
Mesh 4	320052	2507.6	24 min 58s

4. Results and Discussion

4.1. Model validation

Validation was performed to show the accuracy of the model results. Due to a lack of experimental data in the area of AP-SOFC with hydrogen fuel, the results were compared to experimental data provided by Timurkutluk et al. [34] for a dual chamber SOFC using hydrogen as a fuel. The base cell of their study consisted of Ni/YSZ/LSF materials for anode/electrolyte/cathode layers, respectively, at 750°C operating temperature, where this temperature is maintained as the inlet temperature in the current modeling work. The geometrical and thermo-physical data are shown in Tables 1 and 3, respectively.

Fig. 4 shows how the model results for a dual chamber configuration are in agreement with the experimental data. In order to calibrate the model results, the electrochemically active surface area per unit volume at anode and cathode and also the anodic and cathodic charge transfer coefficients were considered as fitting parameters. The current data were obtained with A_a=1.935×10⁶ m²/m³, A_c=1.93×10⁷ m²/m³, α_a=0.25, and α_c=0.875. These fitting parameters were maintained for this study. The input parameters used for validation are tabulated in Table 3.

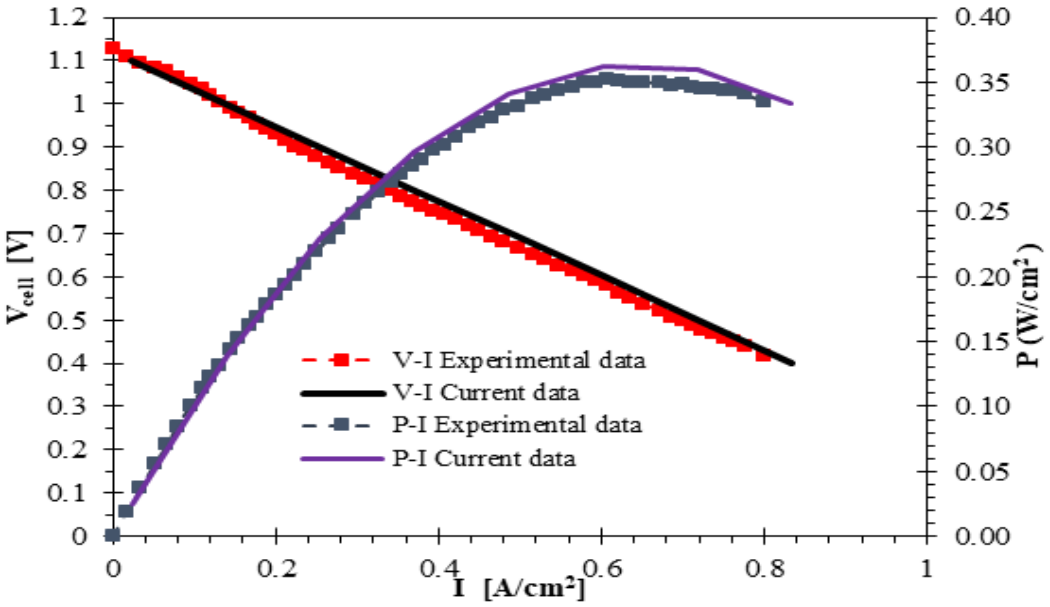

Fig. 4. The current model accuracy applied to a conventional SOFC and compared to Timurkutluk's data.

Table 3. Input parameters used in validation.

Description	Symbol	Value	Dimensions
Inlet velocity	u_{in}	5	m/s
Inlet temperature	T_{in}	1023	K
Total inlet pressure	p_t	1	atm
H_2 inlet molar fraction	x_{0,H_2}	0.97	1
H_2O inlet molar fraction	x_{0,H_2O}	0.03	1
O_2 inlet molar fraction	x_{0,O_2}	0.21	1
N_2 inlet molar fraction	x_{0,N_2}	0.79	1
Inlet velocity	u_{in}	5	m/s
Anode and cathode permeability [43]	κ	10^{-10}	m^2
Anode and cathode porosity [43]	ε	0.4	1
Anode and cathode tortuosity	τ	2.75	1
Universal gas constant	R_u	8.314	J/mol.K
Anode thermal conductivity [18]	k_a	3	W/m.K
Cathode thermal conductivity [18]	k_c	3	W/m.K
Electrolyte thermal conductivity [18]	k_e	2	W/m.K
Anode conductivity [35]	σ_a	71428.57	S/m
Cathode conductivity [35]	σ_c	5376.34	S/m
Electrolyte conductivity [35]	σ_e	0.64	S/m
Anode specific heat [18]	$C_{p,a}$	595	J/kg.K
Cathode specific heat [18]	$C_{p,c}$	573	J/kg.K
Electrolyte specific heat [18]	$C_{p,e}$	606	J/kg.K
Anode density [18]	ρ_a	6870	kg/m^3
Cathode density [18]	ρ_c	6570	kg/m^3
Electrolyte density [18]	ρ_e	5900	kg/m^3
Dynamic viscosity of hydrogen [18]	μ_{H_2}	$6.162\square10^{\square6}+1.145\square10^{\square8}T$	Pa.s
Dynamic viscosity of oxygen [18]	μ_{O_2}	$1.668\times10^{-5}+3.168\times10^{-8}T$	Pa.s
Dynamic viscosity of nitrogen [18]	μ_{N_2}	$1.435Ч10^{-5}+2.642Ч10^{-8}T$	Pa.s
Dynamic viscosity of water [18]	μ_{H_2O}	$4.567\times10^{-6}+2.209\times10^{-8}T$	Pa.s
Thermal conductivity of hydrogen [18]	k_{H_2}	$0.08525+2.964Ч10^{-4}T$	W/m.K
Thermal conductivity of oxygen [18]	k_{O_2}	$0.01569+5.69Ч10^{-5}T$	W/m.K
Thermal conductivity of nitrogen [18]	k_{N_2}	$0.01258+5.444Ч10^{-5}T$	W/m.K
Thermal conductivity of water [18]	k_{H_2O}	$-0.0143+9.782Ч10^{-5}T$	W/m.K

4.2. Comparative study

In this section, a comparative study between two different flow configurations of AP-SOFC: case 1: co-flow configuration and case 2: counter-flow configuration (see Fig. 2) with the same input data is presented. To have a more realistic comparison, all input parameters used in the validation section are maintained. Fig. 5 depicts a comparative performance between 0.3 electrolyte porosity case 1 and case 2 in the same input parameters is given in Table 3 at 750°C operating temperature. Figure 5 reveals that the AP-SOFC with a counter-flow configuration, i.e., case 2, shows better cell performance. The maximum power density produced by case 2 is 2665 W/m^2, while this value for case 1 is 2540 W/m^2, showing a 4.9% increase in maximum power density produced by the cell. It is realized that the counter-flow configuration is the preferred design for the hydrogen-fuelled AP-SOFC scheme. However, both cases produce less maximum power density compared to a conventional SOFC. This value for a conventional SOFC is about 3596 W/m^2. Two key factors play a major role in this low AP-SOFC performance: i) the porous electrolyte displays a lower ionic conductivity, as compared to a dense one because oxide ions are able to diffuse only through the solid portion of the electrolyte and ii) diffusion and transportation of inactive species via the porous electrolyte from anode to cathode and vice versa reduces the cell performance.

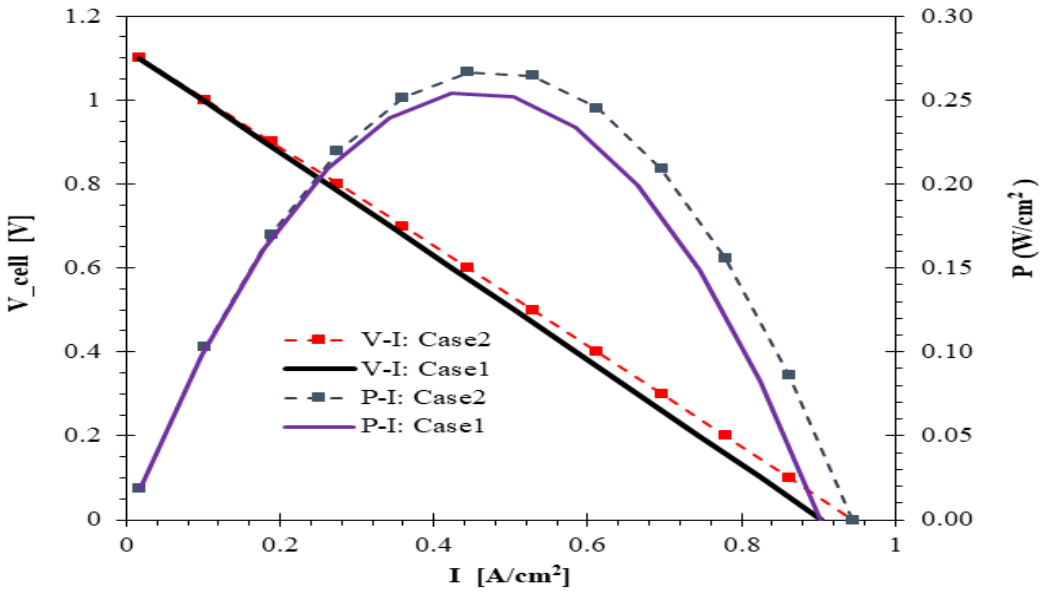

Fig. 5. A comparative performance representation between 0.3 electrolyte porosity, co- and counter-flow config-.urations AP-SOFC with the same input

Fig. 6 shows the distribution of the y component velocity field along the x axis crossing from y=h_{cell}/2, h_{cell}/4, and 3h_{cell}/4 at cell voltage 0.7 V and 750°C operating temperature for cases 1 and 2.

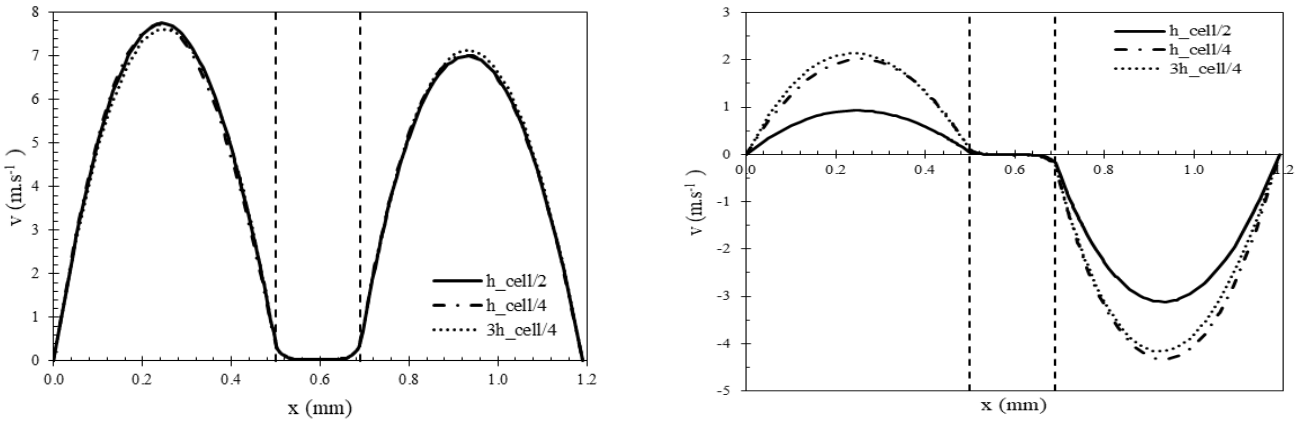

(a) Casel (b) Casel

Fig. 6. y component velocity field distribution along the x axis crossing from y=h_{cell}/2, h_{cell}/4, and 3h_{cell}/4 at cell voltage 0.7 V and a 750°C operating temperature for (a) case 1 and (b) case 2.

It can be seen that the velocity attains a value very close to zero in the all-porous PEN (Positive electrode-Electrolyte-Negative electrode) in both cases. This very low velocity is due to the porous nature of the PEN, causing a very low permeability. This causes the Darcy pressure drop term $\left(-\frac{\mu}{K}\nabla P\right)$ to be very large. However, two different flow behaviors are observed for cases 1 and 2. In case 1, the velocity distribution trends along the x-axis crossing different y positions are the same. Furthermore, the maximum velocity magnitude in anode and cathode channels are 7.76 and 7 m/s, respectively, showing a 10% increase in the maximum velocity for the anode channel. Comparing this value to the inlet velocity (which is equal to 5m/s) shows a 55% and 40% increase in anode and cathode channels, respectively. This big increase in velocity magnitude can lead to a decrease in cell performance by passing unused hydrogen and oxygen from the anode and cathode channels, respectively. Note that this increased value of velocity compared to inlet velocity is due to the boundary layer growth from the channel wall. But in case 2, the velocity value in the middle of the cell is less, and the velocity distribution near the inlet and outlet shows approximately the same. The maximum velocity magnitude in anode and cathode channels are 2 and 4.3 m/s, respectively, showing a 115% increase in the cathode channel of case 2. However, both values are less than the inlet velocity. This means that when the counter-flow configuration is used for an AP-SOFC, the velocity values are less than the inlet velocity, and this helps hydrogen and oxygen to diffuse in anode and cathode reaction zones, respectively, and produce much more electricity.

Figs. 7-9 depict hydrogen, water, and oxygen mole fraction distributions along the y-axis crossing the middle of the represented layer at a cell voltage of 0.7V and 750°C operating temperature for cases 1 and 2. It is realized from Fig. 7a that hydrogen leaves the anode channel of case 2 with a mole fraction of 0.092, while this value for case 1 is 0.7. This shows that more hydrogen is consumed in case 2. However, the existing hydrogen has a mole fraction of 0.7 at the cathode channel outlet, while this value for case 1 is 0.36. The lower mole fraction of hydrogen at the anode channel outlet in case 2 originates from two factors: 1) consumption of hydrogen due to the electrochemical reaction occurring in the anode functional layer and 2) hydrogen leakage within the porous electrolyte into the cathode channel. By comparing hydrogen mole fractions in the anode functional layers of the two cases in Fig. 7b, it is understood that more hydrogen diffuses in the anode functional layer of case 2 decreases from 0.96 to about 0.03, while this decline for case 1 is with a lower slope, decreasing from 0.77 to 0.56. Note the small amount of hydrogen emerging in the anode functional layer of case 2 near the outlet should

be given attention in cases with longer channel length. Fig. 8 shows that more water is produced in case 2. The maximum water mole fraction in case 2 is 0.038, occurring in the anode channel at y=3.5mm. It is also found that more water is produced on the anode side of the cell in case 2 near the inlet, indicating that this portion of the cell is more active in producing electricity. However, a reduction in the water amount in case 1 is observed. Water amount experiences a slight decrease from 0.03 to 0.026 in the anode channel of case 1, while the water amount on the other side shows the opposite behavior, increasing from 0 to 0.01 in the cathode channel of case 1. Oxygen in the cathode channel of both cases 1 and 2 decreases from 0.21 to 0.11 and 0.05, respectively, as shown in Fig. 9a.

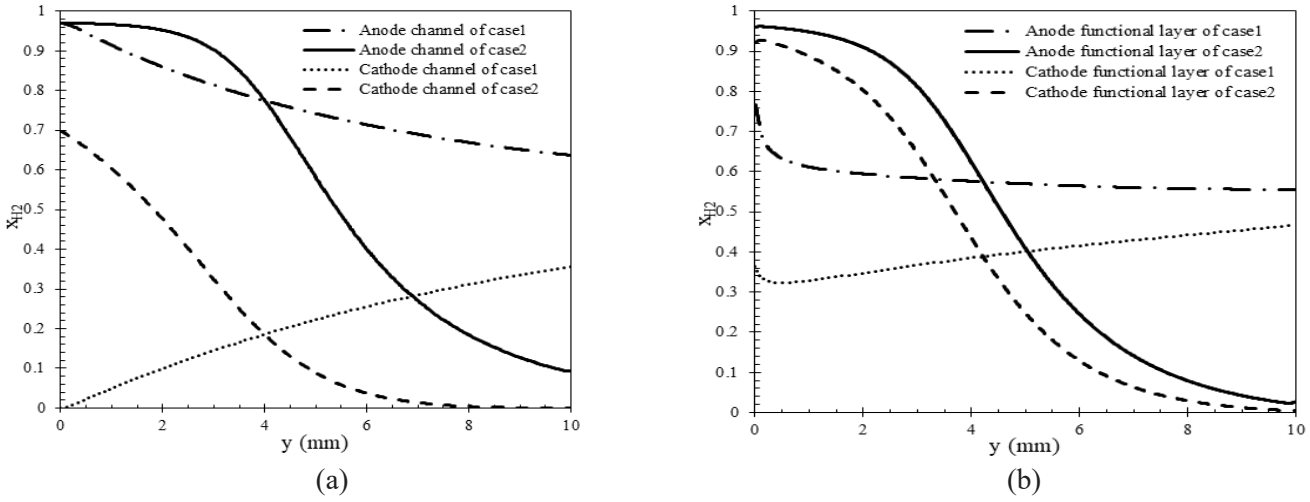

Fig. 7. Hydrogen mole fraction distribution along the y-axis crossing the middle of (a) anode and cathode channels (b) anode and cathode functional layers at cell voltage 0.7 V and 750°C operating temperature for cases 1 and 2.

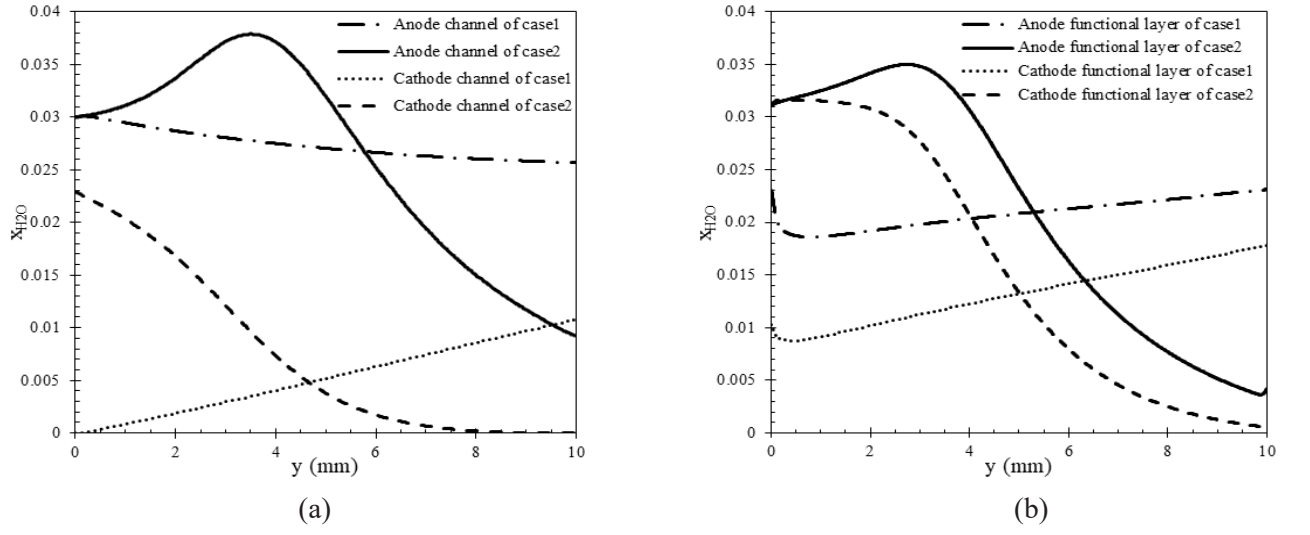

Fig. 8. Water mole fraction distribution along the y-axis crossing the middle of (a) anode and cathode channels (b) anode and cathode functional layers at cell voltage 0.7 V and 750oC operating temperature for cases 1 and 2.

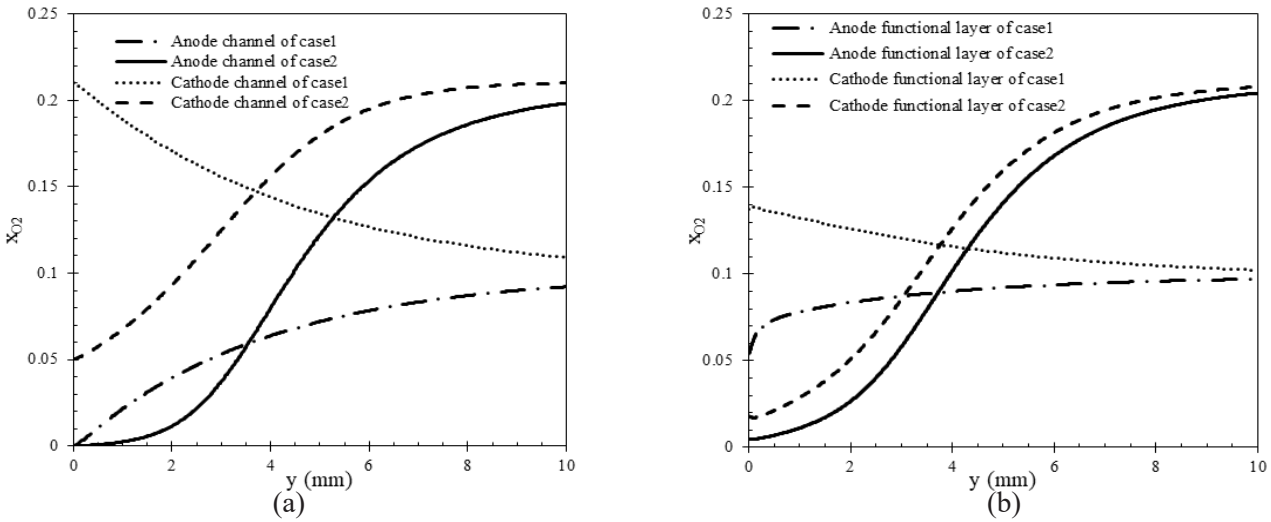

Fig. 9. Oxygen mole fraction distribution along the y axis crossing the middle of (a) anode and cathode channels (b) anode and cathode functional layers at cell voltage 0.7 V and 750oC operating temperature for cases 1 and 2.

A greater reduction of oxygen (76%) in the cathode channel is observed in case 2. Fig. 9b shows that the oxygen emergence in the anode functional layer of case 1 is more uniform and is an obstacle for hydrogen molecules taking part in the electrochemical reaction, while this emergence of oxygen in case 2 is limited to the top half of the cell.

Fig. 10 shows temperature contours for cases 1 and 2 at a cell voltage of 0.5V. As it can be seen, case 2 reveals a higher maximum temperature compared to case 1. The maximum temperature for case 2 is 1041K, while this value for case 1 is 1032.5K. Furthermore, the point of the cell having the maximum temperature is (0.602,5.43) and (0.597,7.508) mm for cases 1 and 2, respectively. This shows that the maximum temperature occurs at the middle of the electrolyte layer in both cases; however, this point for case 2 is closer to the outlet. Furthermore, the temperature distribution in case 1 is more uniform compared to case 2. Thus, case 2 is more probable to crack initiation by thermal stresses, which is not a problem in AP-SOFCs.

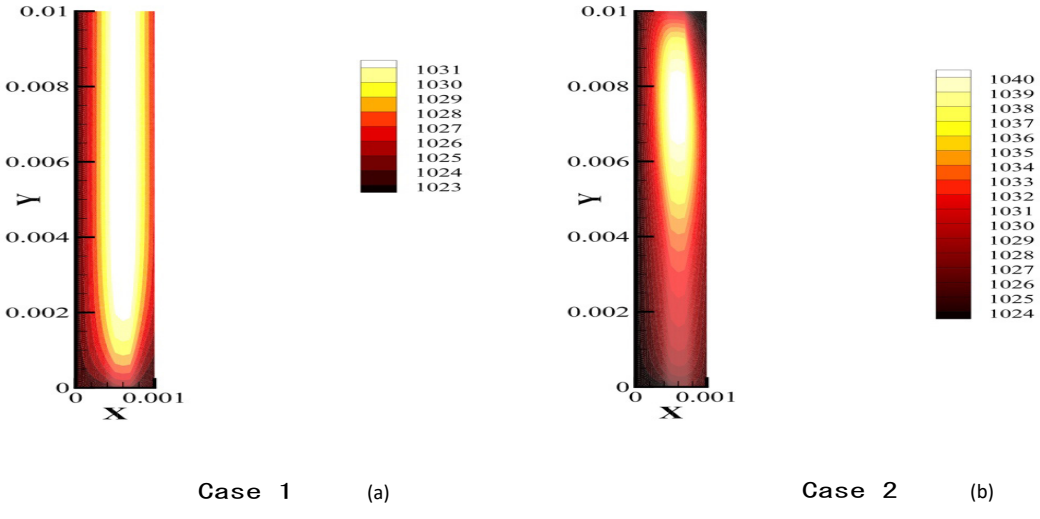

Fig. 10. Temperature contours for cases 1 and 2 at a cell voltage of 0.5V.

5. Conclusions

A comparative numerical study of co- and counter-flow configurations of hydrogen-fuelled planar all-porous solid oxide fuel cell has been performed. Results indicated that the counter-flow configuration is more suitable for an AP-SOFC scheme. The cell with a counter-flow configuration showed a 4.9% increasing in maximum power density produced by the cell compared to the co-flow configuration cell. Furthermore, comparing the velocity field distribution in each channel revealed that the velocity field distribution in the counter-flow configuration differs in each section, while this trend for the co-flow configuration was the same. One of the key factors in the reduction of the AP-SOFC performance as compared to a conventional SOFC is the emergence of 'spectator' species in the functional layers. In the counter-flow configuration, the emergence of 'spectator' species was limited to the end portion of the cell, while in the co-flow configuration, this emergence was spread in all portions. Finally, the counter-flow configuration showed a higher maximum temperature occurred in the middle of the electrolyte.

References

[1] EG and G Technical Services, Inc. Science Applications International Corporation, 6th ed., Fuel Cell Handbook, US Department of Energy,2002 .

[2] Kamvar M., Ghassemi M. and Rezaei M., "Effect of catalyst layer configuration on single chamber solid oxide fuel cell performance", J. Applied Thermal Engineering, 2016, 100: 98.

[3] Kupecki J., Motylinski K., Zurawska A., Kosiorek M. and Ajdys L., "Numerical analysis of an SOFC stack under loss of oxidant related fault conditions using a dynamic non-adiabatic model", Int. J. Hydrogen Energy, 2019, 44: 21148.

[4] El-Hay E.A., . El-Hameed M.A and El-Fergany A.A., "Optimized Parameters of SOFC for steady state and transient simulations using interior search algorithm", J. Energy, 2018, 166: 451.

[5] Moreno-Blanco J., Elizalde-Blancas F., Riesco-Avila J.M., Belman-Flores J.M. and Gallego-Munoz A., "On the effect of gas channels-electrode interface area on SOFCs performance", Int. J. Hydrogen Energy, 2019, 44: 446.

[6] Amiri A., Tang S., Steinberger-Wilckens R. and Tadé M.O.: "Evaluation of Fuel Diversity in Solid Oxide Fuel Cell Systems", Int. J. Hydrogen Energy, 2018, 43: 23475.

[7] Bove R. and Ubertini S., 1th ed., Modeling Solid Oxide Fuel Cells, Methods, Procedures and Technologies, Springer, 2008.

[8] Wang Y., Jiang W., Luo Y., Zhang Y. and Tu Sh., "Evolution of thermal stress and failure probability during reduction and re-oxidation of solid oxide fuel cell", J. Power Sources, 2017, 371: 65.

[9] Hao Y., Shao Z., Mederos J., Lai W., Goodwin D. G. and Haile S. M., "Recent advances in single-chamber fuel cells: Experiment and modeling", Solid State Ionics, 2006, 177: 2013.

[10] Ahn S., Kim Y., Moon J., Lee J. and Kim J., "Influence of patterned electrode geometry on performance of co-planar, single-chamber, solid oxide fuel cell", J. Power Sources, 2007, 171: 511.

[11] Yano M., Tomita A., Sano M. and Hibino T., "Recent advances in single-chamber solid oxide fuel cells: A review", Solid State Ionics, 2007, 177: 3351.

[12] Akhtar N., "Single-Chamber Solid Oxide Fuel Cells: Modeling and Experiments", PhD thesis, University of Birmingham, 2010.

[13] Yano M., Tomita A., Sano M. and Hibino T., "Recent advances in single-chamber solid oxide fuel cells: A review", Solid State Ionics, 2007, 177: 3351.

[14] Akhtar N., Decent S. P. and Kendall K., "Numerical modelling of methane-powered micro-tubular, single-chamber solid oxide fuel cell", J. Power Sources, 2010, 195: 7796.

[15] Hibino T. and Iwahara H., "Simplification of solid oxide fuel cell system using partial oxidation of methane", Chemistry Letters, 1993, 22: 1131.

[16] Kamvar M., Ghassemi M. and Steinberger-Wilckens R., "The numerical investigation of a planar single chamber solid oxide fuel cell performance with a focus on the support types", Int. J. Hydrogen Energy, 2020, 45: 7077.

[17] Chung Ch. Y. and Chung Y. Ch., "Performance characteristics of micro single-chamber solid oxide fuel cell: Computational analysis", J. Power Sources, 2006, 154: 35.

[18] Liu M., Lu Zh., Wei B., Huang X., Zhang Y. and Su W., "Numerical modeling of methane-powered micro-tubular, single-chamber solid oxide fuel cell", J. Power Sources, 2010, 195: 7796.

[19] Akhtar N., Decent S. P., Loghin D. and Kendall K., "A three dimensional numerical model of a single-chamber solid oxide fuel cell", Int. J. Hydrogen Energy, 2009, 34: 8645.

[20] Akhtar N., Decent S. P. and Kendall K., "A parametric analysis of a micro-tubular, single-chamber solid oxide fuel cell (MT-SC-SOFC)", Int. J. Hydrogen Energy, 2011, 36: 765.

[21] Jacques-Bedrad X., Napporn T.W., Roberge R. and Meunier M., "Performance and ageing of an anode-supported SOFC operated in single-chamber conditions", J. Power Sources, 2006, 153: 108.

[22] Morel B., Roberge R., Savoie S., Napporn T. W. and Meunier M., "Temperature and performance variations along single chamber solid oxide fuel cells", J. Power Sources, 2009, 186: 89.

[23] Hao Y. and Goodwin D. G., "Numerical Modeling of Single-Chamber SOFCs with Hydrocarbon Fuels", J. Electrochem. Soc., 2017 154: B207.

[24] Akhtar N. and Kendall K., "Micro-tubular, solid oxide fuel cell stack operated under single-chamber conditions", Int. J. Hydrogen Energy, 2011, 36: 13083.

[25] Akhtar N., "Micro-tubular, single-chamber solid oxide fuel cell (MT-SC-SOFC) stacks: Model development", Chemical Engineering Research and Design, 2012, 90: 814.

[26] Akhtar N., "Modeling of novel porous inserted micro-tubular, single-chamber solid oxide fuel cells (MT-SC-SOFC)", Chemical Engineering Journal, 2012, 179: 277.

[27] Hao Y. and Goodwin D.G., "Efficiency and fuel utilization of methane-powered single-chamber solid oxide fuel cells", J. Power Sources, 2008, 183: 157.

[28] Kong W., Han Zh., Lu S., Gao X. and Wang X., "A novel interconnector design of SOFC", Int. J. Hydrogen Energy, 2020, 45: 20329.

[29] Schluckner C., Subotic V., Preibl S. and Hochenauer C., "Numerical analysis of flow configurations and electrical contact positions in SOFC single cell and their impact on local effects", Int. J. Hydrogen Energy, 2019, 44: 1877.

[30] Moreno-Blanco J., Elizalde-Blancas F., Riesco-Avila J.M., Belman-Flores J.M. and Gallegos-Munoz A., "On the effect of gas channels-electrode interface area on SOFCs performance", Int. J. Hydrogen Energy, 2019, 44: 446.

[31] Guo Y., Bessaa M., Aquado S., Cesar Steil M., Rembelski D., Rieu M., et al., "An all porous solid ocide fuel cell (SOFC): a bridging technology between dual and single chamber SOFCs", Energy Environ. Sci., 2013, 6: 2119.

[32] Xu H., Chen B., Tan P., Xuan J., Mercedes M., et al., "Modelling of all-porous solid oxide fuel cells with a focus on the electrolyte porosity design", Applied Energy, 2019, 235: 602.

[33] Xu H., Chen B., Tan P., Zhang Y., He Q., et al., "The thermal effects of all-porous solid oxide fuel cells", J. Power Sources, 2019, 440: 227102.

[34] Timurkutluk B., Celik S., Timurkutluk C., Mat M.D. and Kaplan Y., "Novel electrolytes for solid

oxide fuel cells with improved mechanical properties", Int. J. Hydrogen Energy, 2012, 37: 13499.

[35] Nield D.A. and Bejan A., 3rd ed., Convection in Porous Media, Springer, 2006.

[36] Ghassemi M., Kamvar M. and Steinberger-wilckens R., 1st ed., Fundamentals of heat and fluid flow in high temperature fuel cells, Elsevier, 2020.

[37] Batchelor G.K., 1st ed., An Introduction To Fluid Dynamics, Cambridge University Press, 2000.

[38] Todd B. and Young J.B., "Thermodynamic and transport properties of gases for use in solid oxide fuel cell modelling", J. Power Sources, 2002, 110: 186.

[39] Taylor R. and Krishna R., 1th ed., Multicomponent mass transfer, John Willey & Sons, Inc., 1993.

[40] Hussain M.M. and Li X., Dincer I., "Mathematical modeling of planar solid oxide fuel cells", J. Power Sources, 2006, 161: 1012.

[41] Janardhanan V.M. and Deutschmann O., "CFD analysis of a solid oxide fuel cell with internal reforming: Coupled interactions of transport, heterogeneous catalysis and electrochemical processes", J. Power Sources, 2006, 162: 1192.

[42] Zhu H., Kee R.J., Janardhanan V.M.. Deutschmann O. and Goodwin D.G., "Modeling elementary heterogeneous chemistry and electrochemistry in solid-oxide fuel cells", J. Electrochem. Soc., 2005, 152: A2427.

[43] Huang K. and Goodenough J.B., 1st ed., Solid oxide fuel cell technology principles, performance and operations, CRC Press, 2009.

[44] Jeon D.H., "A comprehensive CFD model of anode-supported solid oxide fuel cells", Electrochemica Acta, 2009, 54: 2727.

[45] Cengel Y.A., Boles M.A. and Kanoglu M., 9th ed., Thermodynamics: An Engineering Approach, Mc Graw Hill, 2019.

[46] Kaviany M., 2nd ed., Principles of heat transfer in porous media, Springer, 1995.